# Wavefront sensing of x-ray telescopes

Timo Saha[1], Scott Rohrbach[1], Theo Hadjimichael[1], and William W. Zhang[2]
[1] NASA/Goddard Space Flight Center, Code 551, Greenbelt, MD 20771
[2] NASA/Goddard Space Flight Center, Code 662, Greenbelt, MD 20771

## ABSTRACT

Phase Retrieval analysis of off-axis or defocused focal-plane data from telescope optics has been proven effective in understanding misalignments and optical aberrations in normal incidence telescopes. The approach is used, e.g., in commissioning of the James Webb Space Telescope (JWST) segmented primary mirror. There is a similar need for evaluating low-order figure errors of grazing incidence mirrors and nested telescope assemblies. When implemented in these systems, phase retrieval does not depend on normal incidence access to each mirror (shell) surface and, therefore, provides an effective means for evaluating nested x-ray telescopes during integration and test.

We have applied a well-known phase retrieval algorithm to grazing incidence telescopes. The algorithm uses the Levenberg-Marquardt optimization procedure to perform a non-linear least-squares fit of the telescope Point Spread Function (PSF). The algorithm can also retrieve low order figure errors at visible wavelengths where optical diffraction is the dominant defect in the PSF.

In this paper we will present the analytical approach and its implementation for grazing incidence mirrors of the International X-Ray Observatory (IXO). We analyze the effects of low order axial surface errors individually, and in combination on the system PSF at 633 nanometers. We demonstrate via modeling that the wavefront sensing algorithm can recover axial errors (of the grazing incidence mirrors) to a small fraction of the known axial figure errors using simulated PSFs as input data to the algorithm.

**Keywords:** X-ray telescopes, wavefront sensing, phase retrieval

## 1. INTRODUCTION

X-ray radiation can be reflected only in the grazing incidence configuration if high reflection efficiency is required. This leads to unconventional optical components. The mirrors are long shallow cones and the grazing angles of reflection are typically 1 to 3 degrees. The ratio of the central obscuration area to that of the primary mirror is close to unity. The most commonly used telescope design for x-ray astronomy applications is the Wolter type 1 telescope [1], which consists of a parabolic primary mirror and con-focal hyperbolic secondary mirror. In order to build a system that has a useful optical aperture, many coaxial pairs of these primary mirrors and secondary mirrors are nested. A significant drawback of this approach is that normal incidence metrology can only access the innermost surfaces once the mirror system is assembled. Furthermore, to maximize the effective area versus mass, the mirror substrates must be as thin as possible, making the mirror figure susceptible to mount-induced stresses, making the need for accurate figure metrology in the mounted state even more important.

The small grazing angles control the imaging characteristics of the x-ray telescopes. The designs are very sensitive to axial slope errors and insensitive to the circumferential slope errors[2]. Radial image errors are directly proportional to the axial slope errors. The circumferential image errors are proportional to the circumferential slope errors and the grazing angle of the mirror. Therefore, small grazing angles de-magnify the effects of circumferential slope errors in the focal plane.

The International X-Ray Observatory (IXO) project[3] has developed Hartmann techniques[4,5] to measure the radial Point Spread Functions (PSF) across the circumference of the mirror. The technique utilizes a collimated visible-light beam and narrow slit that is scanned across the circumference of the mirror. The centroids of the PSFs are calculated and this

data is then used to evaluate the imaging capability of the mirror. Alignment related errors, cone angle, and radius errors can be retrieved from the centroid data and the best focus of the mirror segment or telescope can be found.

Unfortunately, the grazing incidence configuration of the mirrors enlarges the diffraction effects of the annular aperture in the visible wavelengths complicating the analysis. For example, a radial height of the annular aperture of 2mm spreads the central diffraction peak to 65 arc-sec in the focal plane at a wavelength of 633 nm. In spite of large diffraction effects the measured radial PSFs in the focal plane contain information about the low order surface errors of the mirror.

Phase retrieval analysis of off-axis or defocused images of high quality telescope optics has been proven effective in understanding misalignments and aberrations in normal incidence optical systems, and is being used, for example, for phasing of the James Webb Space Telescope (JWST) segmented primary mirror[6,7,8]. We have developed a phase retrieval technique for grazing incidence telescopes to better understand the low order axial figure errors hidden under the large diffraction effects in the radial PSF.

In this paper we present an analysis of effects of the axial errors of the secondary mirror on the imaging of the mirror. In section 2 we briefly review the analysis technique. In sections 3 and 4 we show how the low order axial errors of the secondary mirror shape the PSF. In section 5 we briefly describe the phase retrieval technique we have developed for the radial image analysis of the grazing incidence mirrors and in section 6 we present preliminary results of our wavefront sensing approach.

## 2. PSF OF SECONDARY MIRROR

Figure 1 illustrates the geometry of the cross-section of a secondary mirror placed in the collimated beam of light. The solid black line represents the hyperbolic secondary mirror. The secondary mirror does not form a stigmatic image at the focal plane. We introduce a reference parabola shown as a dashed line in Figure 1. The axial centers of the parabola and hyperbola have the same radial height. The focus of the parabola is located at the best focus of the secondary hyperbola. The incoming collimated beam is focused by the reference parabola at the best focus of the secondary. The parabola sends out a spherical wavefront towards the focus. The reference sphere can now be located at a distance R from the focus of the mirror. It intersects the reference parabola and secondary hyperbola at the axial midpoint of the mirror.

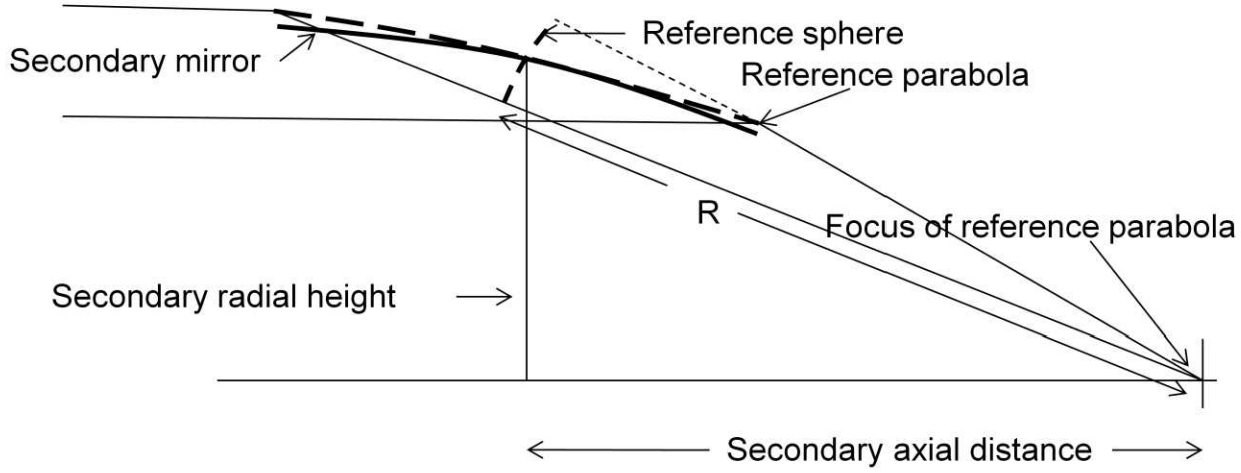


**Figure 1. Cross-section of hyperbolic secondary mirror.**

The optical path difference (OPD) for the grazing incidence configuration can be defined by[9]:

$$OPD(r) = 2\,Dr(z)\sin(\alpha(z)), \quad (1)$$

where $Dr(z)$ is the radial height difference between the reference parabola and the hyperbola and $\alpha$ is the grazing angle of the reference parabola. $Dr(z)$ and $\alpha(z)$ are functions of the axial coordinate $z$ of the reference parabola. The $OPD(r)$ is given in the coordinate system of the reference sphere.

The axial surface errors of the hyperbola can be added to the axial errors between the hyperbola and the reference parabola. If the secondary mirror has axial errors, then the total axial error *Dr* will be

(2)

where *Drp(z)* is the axial error between the reference parabola and the hyperbola and the *Drs(z)* is the axial error of the secondary mirror.

The radial 1-dimensional Point Spread Function (*PSF*) is calculated from the diffraction integral

— — , (3)

where λ is the wavelength of the light beam, *OPD(r)* is calculated from equations (1) and (2), ξ is the radial image plane coordinate, and R is the radius of the reference sphere .

## 3. RADIAL PSF OF SECONDARY MIRROR AND REFERENCE PARABOLA

For this study we have chosen one of the mirror shells from the IXO engineering model telescope. The diameter of the shell is approximately 485 mm and the focal length is 8.4 m. In this paper we present the analysis of the secondary mirror only. The axial length of the secondary mirror shell is 200 mm and the radial width of the annulus is 4.5 mm. The radial height of the secondary mirror at the midpoint of the surface is 240 mm. The secondary mirror focuses a collimated beam about 5529 mm from the midpoint of the surface. The RMS image size at the focus is about 2.2 mm or 84 arc-sec.

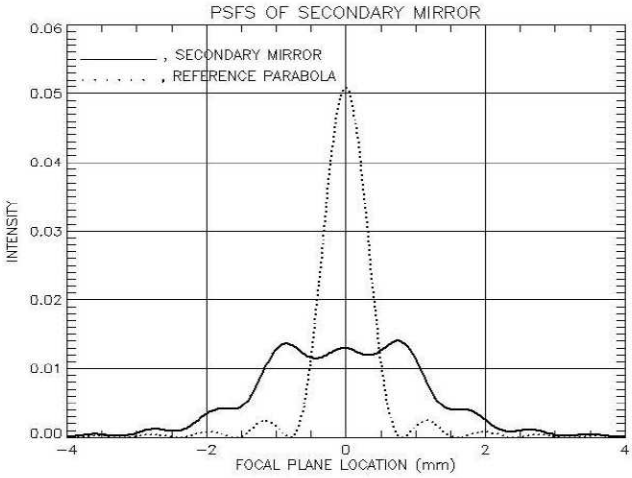


**Figure 2. PSFs of reference parabola and hyperbolic secondary.**

The reference parabola defined in Figure 1 focuses the collimated beam at the focus of the parabola. The radial PSF of the reference parabola can be calculated from Equations (1) and (3). The dotted line in Figure 2 represents the PSF of the reference parabola calculated at a wavelength of 633 nm. The PSF is simply the diffraction image of a slit with a height matching the radial width of the reference sphere. The central peak is about 1.4 mm (52 arc-sec) wide.

The solid line in Figure 2 represents the radial PSF of the secondary hyperbola. The aberrations of the hyperbola lower and broaden the peak. The diffraction maxima and minima are visible in the image and they roughly match the locations of the maxima and minima of the slit image.

## 4. PSFS OF LOW ORDER ERRORS OF SECONDARY MIRROR

The axial figure errors can be added to the OPD using Equation (2) and the resulting PSF can be calculated from Equation (3). We use Legendre polynomials as mirror surface error descriptors[6]. For example, the second order sag error is represented by the second order Legendre polynomial, 3rd order Legendre polynomial is used for 3rd order profile errors, and so on.

Figure 3 shows how the shape of the PSF changes when second order errors are added to the secondary hyperbola. If the amplitude of the second order error is zero (no error), the central part of the PSF has 3 peaks consisting of central maximum and first diffraction maxima on both sides. The PSF is not symmetric because the radial height between the secondary hyperbola and the reference parabola is not symmetric about the midpoint of the mirror.

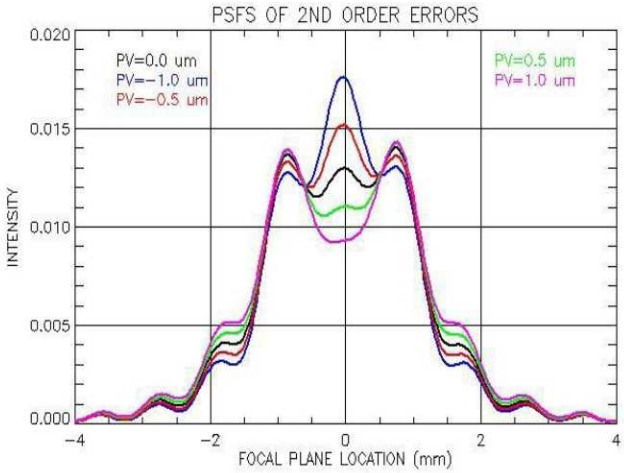


**Figure 3. PSFs of second order errors.**

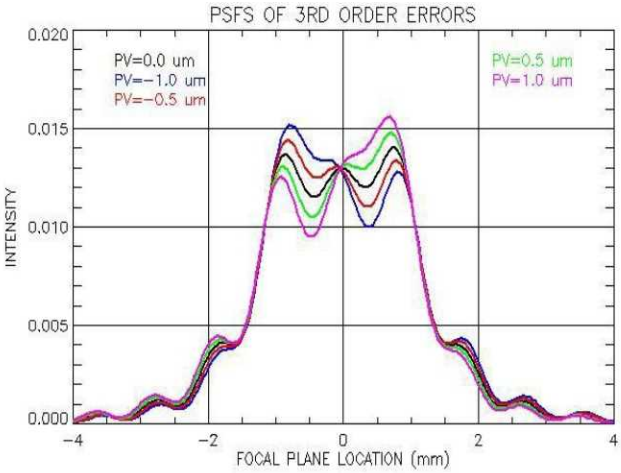


**Figure 4. PSFs of third order errors.**

If the Peak-to-Valley (PV) amplitude of the second order error is negative the central diffraction peak increases and the secondary and tertiary peaks decrease. The PSF is visibly unchanged at the locations of the 4th and higher order peaks. If the amplitude of the second order error is positive the central maximum decreases and first and higher order maxima increase.

The effects of the 3rd order errors are illustrated in Figure 4. The shape of the PSF is considerably different. The height of the central maximum does not change when the PV amplitude of the error is changed. If the PV amplitude is positive the first order maximum on the right side comes up and the first and second order maximum on the left side are suppressed. Positive amplitudes increase the secondary maximum on the left side and flatten the second order maximum on right side. Negative amplitudes have the opposite effect on the secondary maxima. The effects of the 3rd order errors on the tertiary maxima are similar, but the changes of the PSF are smaller.

Figure 5 illustrates the PSF changes caused by 4th order axial errors. The 4th order Legendre polynomial has opposite effect on the central peak and first order maxima. Tertiary diffraction maxima stay unchanged. The 4th order maxima increase when the peak-to-valley amplitude increases. Small changes in the PSF can be also seen in the 5th order diffraction maxima.

Figure 6 shows the changes of the PSF caused by 5th order Legendre polynomial added on the surface of the secondary mirror. As in the case of the 3rd order errors, the changes are not symmetric about the center of the PSF. The central peak stays nearly unchanged. Depending on the sign of the PV amplitude, the first order diffraction maxima increase or decrease the

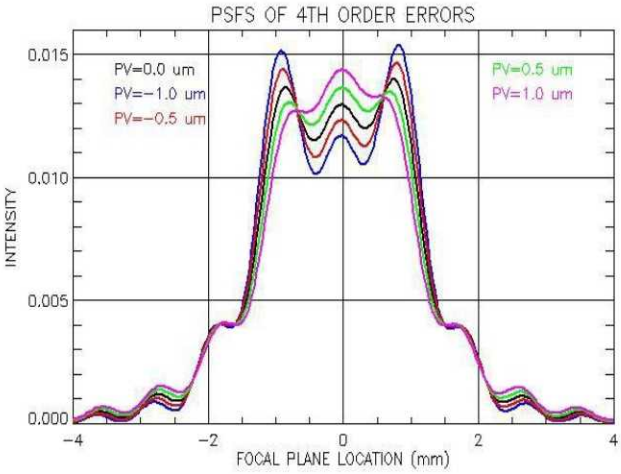


**Figure 5. Effects of fourth order errors on PSF.**

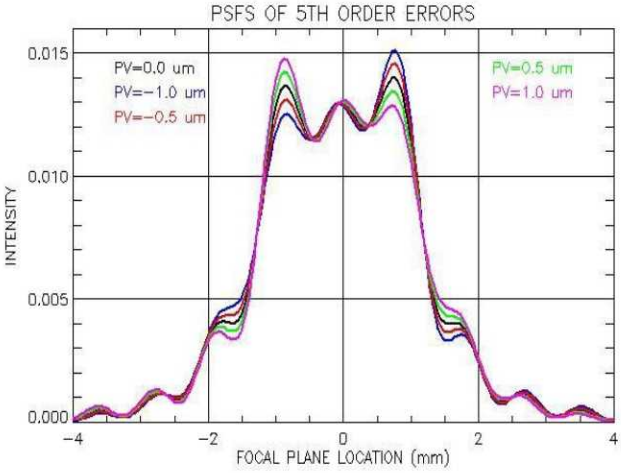


**Figure 6. PSFs of fifth order errors.**

opposite ways. The change in the second order diffraction maxima is also opposite on both sides of the peak. The changes in the 2nd order maxima are opposite to the changes in the 1st order maxima. Small changes are also seen in the 3rd and 4th order maxima.

The changes of the PSF caused by 6th order Legendre surface errors are illustrated in Figure 7. The changes are roughly symmetric about the center of the PSF. The central peak and 1st order diffraction maxima change opposite directions when the surface error is increased or decreased. Positive PV amplitude of the 6th order error flattens out the 2nd, 3rd, and 4th order diffraction maxima and negative amplitude brings up the maxima.

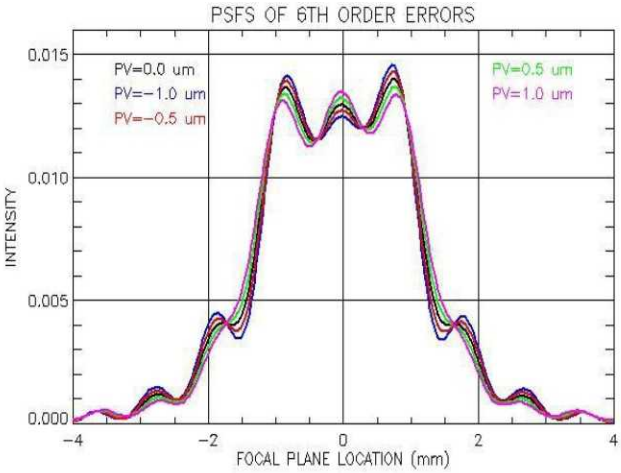


**Figure 7. PSFs of sixth order errors.**

The PSFs plots of low order surface errors added to the secondary mirror indicate that axial figure errors on the order of a micron to one tenth of a micron should be easily recoverable from the PSF. Second order errors redistribute the energy closer the central peak and the changes in the PSF are large. On the other hand, sixth order errors scatter the energy to higher orders and the changes in the PSF will be more difficult to retrieve.

## 5. PHASE RETRIEVAL ALGORITHM

We have developed a phase retrieval algorithm for grazing incidence telescopes. The algorithm approach is based on the Non-Linear Optimization (NLO) method[10] using the Levenberg-Marquardt (LM) least squares fitting of the Point Spread Function (PSF)[11, 12]. The algorithm can retrieve low order axial figure errors of a grazing incidence mirror even at visible wavelengths where optical diffraction is the dominant defect in the PSF.

The implemented LM algorithm generates PSF models calculated from Equation (3) using coefficients of the Legendre polynomials as inputs. The generated PSFs are compared with the measured PSFs. The parameters of the figure error (coefficients of the Legendre polynomials) are adjusted until a good match is found. The routine minimizes the difference between the squares of the amplitudes of the simulated or measured PSF and PSF fit.

## 6. WAVEFRONT SENSING EXAMPLES

The fabricated IXO mirror segments are typically 30 to 50-degrees wide in the azimuthal direction and 200 mm long in the axial direction. From a typical mirror segment fabricated for the IXO development program we have selected 3 axial profiles to demonstrate the phase retrieval process. The solid line in Figure 8 shows a measured axial profile of the mirror segment. The profile is concave consisting of 2nd and higher order axial errors. The PV of the error is about 0.5 μm. This profile has also high spatial frequency components.

From the axial figure error shown in Figure 8 we calculated the OPD and PSF using Equations (1) – (3). The dashed line in Figure 9 represents the resulting model PSF. This PSF was used as an input to our phase retrieval algorithm. In the retrieval process we first adjust the wavefront first order and second order terms (tilt and lowest order curvature) to roughly match the location and

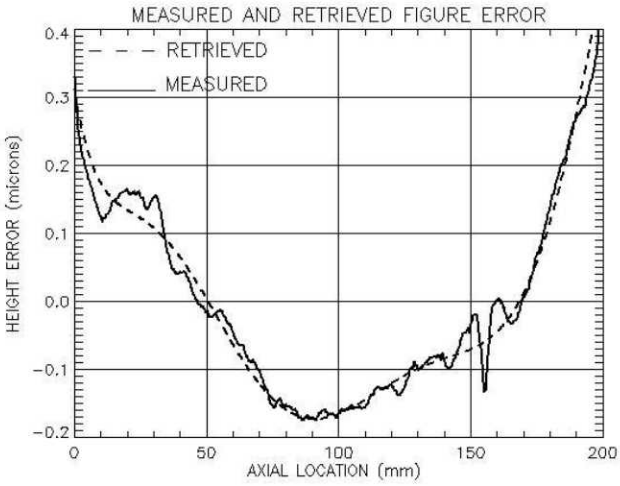


**Figure 8. Measured profile of IXO mirror segment and retrieved profile of example 1.**

shape of the PSF. The algorithm then adds higher order Legendre polynomials one at the time up to $6^{rh}$ order polynomial and finds the optimum Legendre coefficients.

The solid line in Figure 9 shows the retrieved PSF. Visibly, the retrieved PSF matches the original PSF perfectly. The dashed line shown in Figure 8 represents the recovered figure error. The retrieved figure error matches the low orders of the original figure error well. The RMS difference between the profiles is 0.019 μm. High spatial frequency components of the measured profile significantly increase the RMS difference between the measured and recovered profiles and are the dominant difference.

Another example of the retrieval process is shown in Figures 10 and 11. In this example the figure error (solid line) is convex. The top and bottom ends of the profile curl up. This profile has also high spatial frequency components. The resulting model PSF and retrieved PSF are shown in Figure 11. Slight differences can be seen especially at the locations of diffraction maxima and minima. The retrieved figure error shown in Figure 10 matches well the low order contour of the measured profile. High spatial frequency components of the measured profile are not retrieved because only $6^{th}$ order Legendre polynomials were used in the retrieval process. The RMS of the difference between the profiles is 0.021 μm.

The measured axial figure error of our third example is shown in Figure 12. The measured profile was smoothened by fitting the profile to $7^{th}$ order Legendre polynomials. The model PSF and the PSF fit are shown in Figure 13. Again, the model PSF and PSF fit match visibly very well. The retrieved figure error shown in Figure 12 matches the general features of the original figure error fairly well. The RMS of difference between the profiles is 4 nm .

## 7. CONCLUSIONS

The presented analysis demonstrates that phase retrieval techniques can be very useful analysis tools for x-ray optics. Low axial order errors of the mirrors can be recovered from the model PSFs to a small fraction of the figure error.

The analysis tools and wavefront sensing technique we have developed for x-ray grazing incidence mirrors show that the technique works even in visible wavelengths where the aperture diffraction is the dominating defect in the image. From the profiles composed of low order axial errors the technique can retrieve the surface errors to within a few nanometers. We believe that the accuracy of

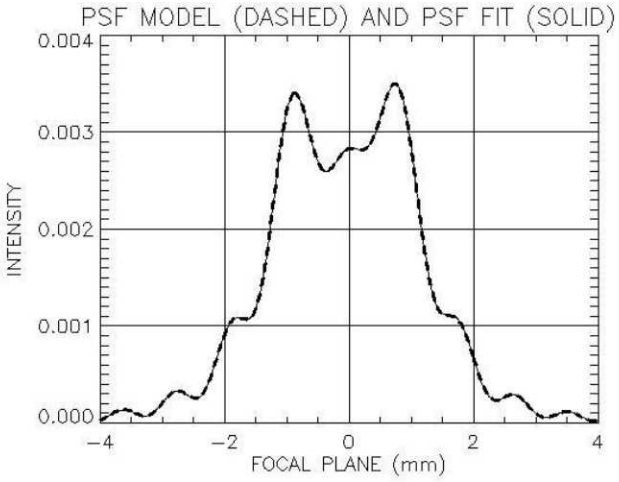


**Figure 9. Model PSF and PSF fit of the first example.**

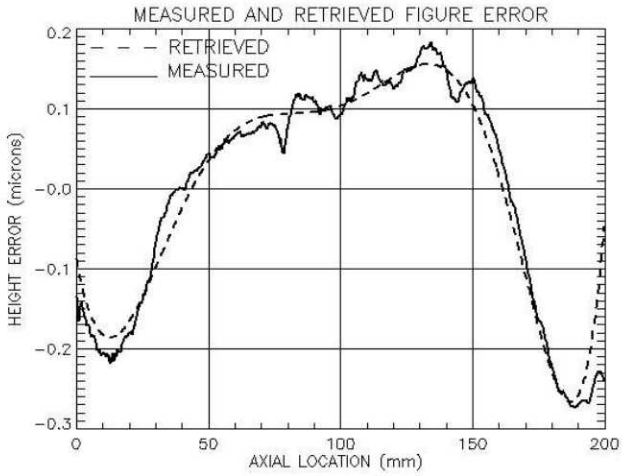


**Figure 10. Measured and retrieved axial profile of IXO mirror segment.**

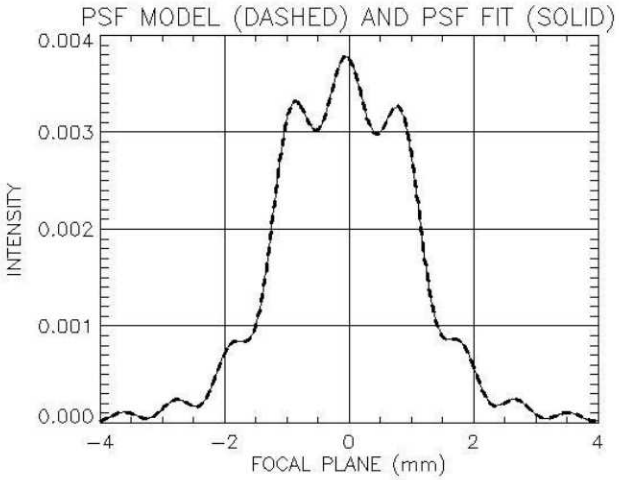


**Figure 11. Model PSF calculated from the figure error of Figure 10 and PSF fit.**

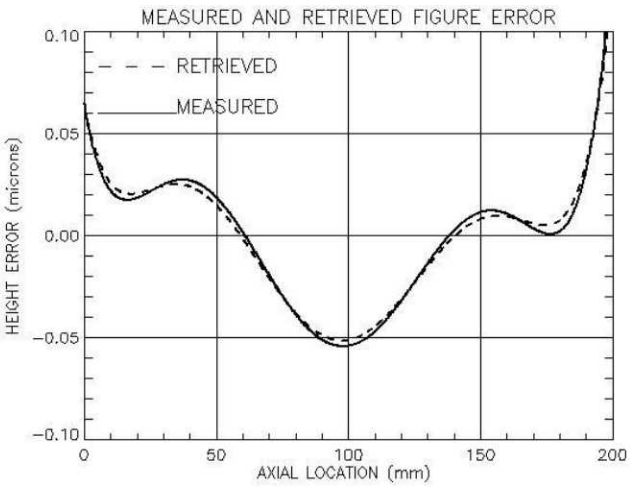


**Figure 12. Measured profile of the IXO mirror segment and retrieved profile.**

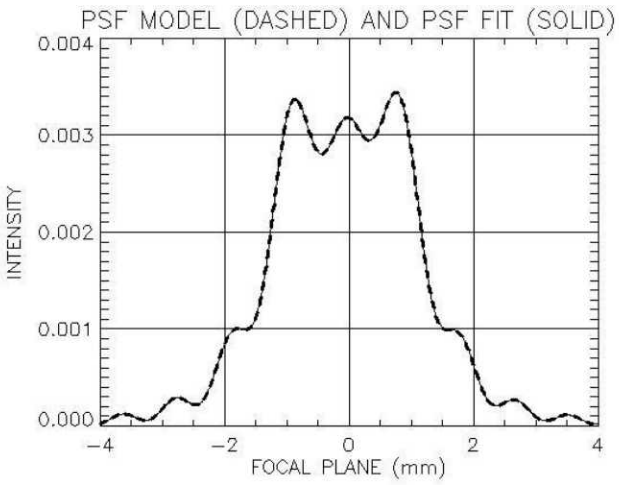


**Figure 13. Model PSF calculated from the profile shown in Figure 12 and PSF fit.**

the technique could be significantly improved if the wavelength of the measurements would be lowered, for example, to the ultraviolet region. Lowering the wavelength would reduce the effects of aperture diffraction and enhance the effects of the surface errors.

The metrology of grazing incidence segmented mirrors is extremely difficult because of the asymmetric nature of the mirrors. Wavefront sensing techniques provide an easy and complimentary way of testing the mirrors.

Metrology approaches based on wavefront sensing do not depend on normal incidence access to the surface of each mirror shell and, therefore, provides an easy way of evaluating highly nested x-ray telescopes during the assembly and integration process and in the evaluation of the image quality of the telescope after the launch into space.

## 8. ACKNOWLEDGEMENTS

This work has been financially supported in part by NASA Astronomy and Physics Research and Analysis (APRA) grant 07-APRA07-0142 and International X-Ray Observatory Project office at Goddard Space Flight Center.

## REFERENCES

[1] Hans Wolter, “Mirror systems with glancing incidence as image producing optics for x-rays,” Ann. .Phys., 10, 94-114 (1952).

[2] Timo T. Saha,”Image defects from surface and alignment errors in grazing incidence telescopes,” Opt. Eng, 29, 1296-1305 (1990).

[3] J. Bookbinder, R. Smith, A. Hornschemeier, et al, “The Constellation-X Observatory,” Proc. SPIE 7011, 701102 (2008).

[4] Tyler Evans, Kai-Wing Chan, and Timo T. Saha, “Arc-Second Alignment of International X-Ray Observatory Mirror Segments in a Fixed Structure,” 2010 IEEE Aerospace Conference Proceedings, March 7–14 ( 2010).

[5] Theo Hadjimichael, Scott Owens, John Lehan, Larry Olsen, Timo Saha, Tom Wallace, and Will Zhang, “An alignment and integration technique for mirror segment pairs on the Constellation-X telescope,” Proc. SPIE 6688, 66881D (2007).

[6] B. H. Dean, D. L. Aronstein, J. S. Smith, R. Shiri, and D. S. Acton , "Phase retrieval algorithm for JWST Flight and Testbed Telescope," Proc. SPIE 6265, 626511(2006)

[7] B. H. Dean, “Looking at Hubble through the Eyes of JWST,” IEEE Aerospace Conference, ISBN: 1- 4244-0525-4 (2007)

[8] J. S. Smith, D. L. Aronstein, B. H. Dean, D. Scott Acton, "Phase retrieval on broadband and under-sampled images for the JWST testbed telescope," Proc. SPIE 7436, 74360D (2009)

[9] Paul Glenn,"Set of orthonormal surface error descriptors for near-cylindrical optics," Opt.Eng. 23, 384-390 (1984).

[10] J.R. Fienup, "Phase Retrieval Algorithms: A Comparison," Appl. Opt. 21, 2758-2769 (1982).

[11] K. Levenberg, "A Method for the Solution of Certain Problems in Least Squares, " Quart. Appl. Math. 2, 164–168 (1944).

[12] D.Marquardt, "An Algorithm for Least Squares Estimation on Nonlinear Parameters," SIAM J. APPL. MATH.11, 431–441(1963).